Quantum simulation of nonequilibrium dynamics and thermalization in the Schwinger model

Wibe A. de Jong[1,*] Kyle Lee,[2,3,†] James Mulligan,[2,3,‡] Mateusz Płoskoń[2,§]
Felix Ringer,[2,‖] and Xiaojun Yao[4,¶]

[1]*Computational Research Division, Lawrence Berkeley National Laboratory,*
Berkeley, California 94720, USA
[2]*Nuclear Science Division, Lawrence Berkeley National Laboratory, Berkeley, California 94720, USA*
[3]*Physics Department, University of California, Berkeley, California 94720, USA*
[4]*Center for Theoretical Physics, Massachusetts Institute of Technology,*
Cambridge, Massachusetts 02139, USA

We present simulations of nonequilibrium dynamics of quantum field theories on digital quantum computers. As a representative example, we consider the Schwinger model, a $(1 + 1)$-dimensional U(1) gauge theory, coupled through a Yukawa-type interaction to a thermal environment described by a scalar field theory. We use the Hamiltonian formulation of the Schwinger model discretized on a spatial lattice. With the thermal scalar fields traced out, the Schwinger model can be treated as an open quantum system and its real-time dynamics are governed by a Lindblad equation in the Markovian limit. The interaction with the environment ultimately drives the system to thermal equilibrium. In the quantum Brownian motion limit, the Lindblad equation is related to a field theoretical Caldeira-Leggett equation. By using the Stinespring dilation theorem with ancillary qubits, we perform studies of both the nonequilibrium dynamics and the preparation of a thermal state in the Schwinger model using IBM's simulator and quantum devices. The real-time dynamics of field theories as open quantum systems and the thermal state preparation studied here are relevant for a variety of applications in nuclear and particle physics, quantum information and cosmology.

I. INTRODUCTION

Quantum computing has emerged in recent years as a promising approach to solve a variety of classically intractable problems, due to considerable progress in hardware and algorithms [1–4]. In particular, *quantum simulations* of real-time dynamics of systems where the classical computational cost scales exponentially with the system size may become tractable in the near or midterm future [5,6]. In high-energy and nuclear physics, a number of quantum computing applications have been proposed [7–30]. For applications in quantum field theories (QFTs), the Hamiltonian formulation of field theories [31] leads to exponentially large Hilbert spaces such that simulations may only become feasible with the advancement of quantum computing. In Refs. [32–35], it was shown that

scattering processes in scalar and purely fermionic field theories can be simulated efficiently with quantum computers, and they belong to the bounded-error quantum polynomial time complete complexity class. Significant progress toward simulating field theories with quantum computing has been made over the past decade. Together with algorithmic advancements, first computations of quantum field theories for closed systems have been performed using real quantum devices [36–55]. See also Refs. [56–58] for recent reviews.

For most applications, it is crucial to prepare the initial state efficiently, which often is the ground state for real-time evolution in vacuum or a thermal state for real-time dynamics at finite temperature. Several approaches have been proposed to prepare a thermal state such as the quantum Metropolis algorithm [59], the imaginary time evolution method [60], and the coupling with a heat bath [61–64]. The last approach that is based on open quantum system formalism, or more generally, nonequilibrium dynamics of quantum systems, plays an important role in many physical systems. Open quantum systems are relevant in high-energy and nuclear physics [65–81], cosmology [82–86], dark matter [87], and quantum information science [88]. In particular, in

*wadejong@lbl.gov
†kylelee@lbl.gov
‡james.mulligan@berkeley.edu
§mploskon@lbl.gov
‖fmringer@lbl.gov
¶xjyao@mit.edu

ultrarelativistic heavy-ion collisions, probes of the quark-gluon plasma such as heavy quark bound states or jets can be described as open quantum systems [65–78]. These studies are also closely related to the more general question on how the early stages of heavy-ion collisions form a quark-gluon plasma that is close to thermal equilibrium [89].

In this paper, we carry out quantum simulations of open systems described by QFTs for the first time. We consider a $(1 + 1)$-dimensional U(1) gauge theory, the Schwinger model [90,91], as the open system coupled to a thermal environment consisting of scalar fields in $1 + 1$ dimensions. The Schwinger model serves as a compelling example for our studies as it exhibits several features which are also present in quantum chromodynamics (QCD), such as confinement and spontaneous chiral symmetry breaking [92–95]. Due to its relative simplicity and important role in improving our understanding of more complex theories such as QCD, various studies have recently been carried out to investigate the real-time dynamics of the Schwinger model as a closed system [40,41,43,47,48]. More recently, thermalization dynamics of the Schwinger model was studied on an analog quantum computer [96]. In this work, we set up the relevant formalism to study field theoretical nonequilibrium dynamics. This formalism represents an important step toward studies of real-time dynamics of QCD in a thermal environment. In addition, we present results using the digital quantum devices accessible through the IBM Quantum (IBMQ) platform. Also, our study demonstrates a method for preparing an initial thermal state—an essential ingredient in applications of quantum computing to systems at finite temperature.

II. DISCRETIZED HAMILTONIAN OF THE SCHWINGER MODEL

The Lagrangian of the (massive) Schwinger model is given by [90,91]

$$\mathcal{L} = \bar{\psi}(i\slashed{D} - m)\psi - \frac{1}{4}F^{\mu\nu}F_{\mu\nu}, \qquad (1)$$

where $\slashed{D} = \gamma^\mu D_\mu$ with $\{\gamma^\mu, \gamma^\nu\} = 2g^{\mu\nu}$, the covariant derivative is $D_\mu = \partial_\mu - ieA_\mu$ and the field strength tensor is $F_{\mu\nu} = \partial_\mu A_\nu - \partial_\nu A_\mu$. The fermion field has two components $\psi = (\psi_u, \psi_d)^T$, where u, d represent the upper and lower components, respectively. Furthermore, m and e denote the mass and the charge of the fermion, respectively.

To simulate the real-time dynamics of the Schwinger model on a quantum computer, we employ the Kogut-Susskind Hamiltonian formulation of Ref. [31] and discretize the field theory on a spatial lattice with N sites. We employ periodic boundary conditions, which allows for the projection onto a reduced Hilbert space with definite momentum and parity. From the Lagrangian in Eq. (1), the discretized Hamiltonian can be obtained by choosing the axial gauge

$A_0 = 0$, using staggered fermions [31,97,98] and applying the Jordan-Wigner transformation [99], which is reviewed in Appendices A and B in detail. The Hamiltonian can then be written as

$$H_S = \frac{1}{2a}\sum_{n=0}^{N_f-1}(\sigma^+(n)L_n^-\sigma^-(n+1) + \sigma^+(n+1)L_n^+\sigma^-(n))$$
$$+ \sum_{n=0}^{N_f-1}\left(\frac{ae^2}{2}\ell_n^2 + m(-1)^n\frac{\sigma_z(n)+1}{2}\right), \qquad (2)$$

where a is the lattice spacing, n labels the fermion lattice sites and $N_f = 2N$ is the total number of fermion lattice sites. See Fig. 1 for an example with $N_f = 8$. The continuum theory is recovered in the limits $a \to 0$ and $N_f \to \infty$, such that aN_f is fixed. Here $\sigma^\pm(n) = (\sigma_x(n) \pm i\sigma_y(n))/2$ and $\sigma_{x,y,z}(n)$ are the Pauli matrices at fermion site n. The operators $L_n^\pm$ are the raising/lowering operators for a quantum system with the eigenstates $|\ell_n\rangle$ associated with the eigenvalues ℓ_n. The eigenvalues ℓ_n correspond to the electric flux between the fermion sites n and $n+1$ while the ladder operators $L_n^\pm$ correspond to the gauge link between n and $n+1$, which increases or decreases the electric flux by one unit. The subscript S of the Hamiltonian in Eq. (2) indicates that the Schwinger model will serve as the system interacting with a thermal environment, see Eq. (4) below.

The lattice formulation of the Schwinger model varies in literature in how the infinite number of states of the gauge field are treated. Here we follow the setup of Ref. [43], where a finite-dimensional representation of the gauge degrees of freedom is achieved by imposing a cutoff on the total electric flux. We find the following closed form for the number of physical states that satisfy Gauss's law with $|\ell_n| \leq 1$,

$$\sum_{M=1}^N \frac{2N}{M}\sum_{K=0}^{N-M}\binom{M-1+K}{M-1}\binom{2N-2K-M-1}{M-1} + 3, \qquad (3)$$

which is derived in Appendix C. In the following, we will focus on the Hilbert space projected onto positive-parity
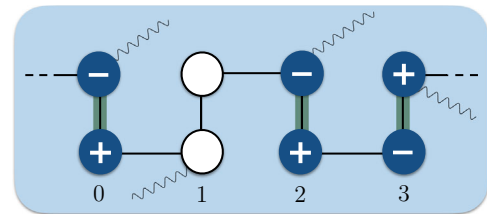

FIG. 1.   Illustration of an example state in the Schwinger model with four spatial lattice sites (eight fermion sites). Empty circles indicate unoccupied sites while a circle with $-(+)$ represents a fermion site occupied by an electron (positron). The electric field is indicated by the green lines between occupied fermion sites. The wavy lines represent interactions with the environment. The dashed end points indicate periodic boundary conditions.

and zero-momentum states with $|\ell_n| \leq 1$ and $\sum_n |\ell_n| < N_f$. Constructions of these states and the matrix forms of the relevant Hamiltonians and measurement operators can be found in Appendix B.

III. NONEQUILIBRIUM DYNAMICS IN THE QUANTUM BROWNIAN MOTION LIMIT

We now consider the Schwinger model coupled to a thermal environment. The full Hamiltonian can be decomposed as

$$H = H_S + H_E + H_I, \tag{4}$$

where H_S denotes the Hamiltonian of the system, i.e. the Schwinger model given in Eq. (2), H_E is the environment Hamiltonian, and H_I describes the interaction between the two. We take the environment to be a thermal scalar field theory and the coupling to the system to be a Yukawa-type interaction:

$$H_E = \int dx \left[\frac{1}{2}\Pi^2 + \frac{1}{2}(\nabla\phi)^2 + \frac{1}{2}m_\phi^2\phi^2 + \frac{1}{4!}g\phi^4 \right], \tag{5}$$

$$H_I = \lambda \int dx\, \phi(x)\bar{\psi}(x)\psi(x) = \int dx\, O_E(x)O_S(x), \tag{6}$$

where $g > 0$ and we define $O_E(x) = \lambda\phi(x)$ and $O_S(x) = \bar{\psi}(x)\psi(x)$.

We assume that the interaction H_I is weak and that the environment is large enough that its change is negligible over the typical relaxation time of the system, i.e. we use the Markovian approximation. Then the full density matrix describing the system and the thermal environment factorizes $\rho(t) = \rho_S(t) \otimes \rho_E$, where $\rho_E = e^{-\beta H_E}/\mathrm{Tr}_E e^{-\beta H_E}$. After tracing out the environmental degrees of freedom, the time evolution of the system density matrix $\rho_S = \mathrm{Tr}_E[\rho]$ is governed by a Lindblad equation [100–102].

Furthermore, we consider the quantum Brownian motion limit, which is valid when the environment correlation time τ_E is hierarchically smaller than both the relaxation time τ_R and the intrinsic timescale τ_S of the system [77]. The condition $\tau_E \ll \tau_R$ is the Markovian condition mentioned above which is valid when H_I is weak. The condition $\tau_E \ll \tau_S$ is equivalent to the hierarchy between the environment temperature T and the characteristic energy gap of the system ΔE_S: $T \gg \Delta E_S$. For QFTs, generally $\Delta E_S \to 0$ in the continuum. The Schrödinger-picture Lindblad equation for the Schwinger model in the quantum Brownian motion limit can be written as

$$\frac{d\rho_S(t)}{dt} = -i[H_S, \rho_S(t)] + L\rho_S(t)L^\dagger - \frac{1}{2}\{L^\dagger L, \rho_S(t)\}, \tag{7}$$

which can be interpreted as a field theoretical Caldeira-Leggett equation [103] by dropping some of the higher

order terms in the expansion of τ_E/τ_S. The corresponding Lindblad operator is given by

$$L = \sqrt{aN_f D}\left(O_S - \frac{1}{4T}[H_S, O_S] \right), \tag{8}$$

where D is a function of T, m_ϕ, g and λ, given by

$$D = \lambda^2 \int dt\, dx\, \mathrm{Tr}_E(\rho_E\phi(t,x)\phi(0,0)). \tag{9}$$

The D term is a two-point correlation function of the environment in momentum space. Here the frequency and momentum of the D term are both zero. The frequency is zero because in the quantum Brownian motion limit, the energy gap is much smaller than the temperature, which allows an expansion in the ratio of the energy gap and the temperature. The momentum is also zero since here we focus on the Hilbert space consisting of only zero momentum states and thus there is no momentum transfer in dynamical processes. In principle, one can calculate the environment correlation function, i.e. the D term, by using thermal scalar field theory. Since it is independent of both frequency and momentum, we simply treat D as an input parameter in the following numerical studies. From Eq. (6), we find $O_S = 1/(2aN_f)\sum_n(-1)^n(\sigma_z(n) + 1)$. Further details of the open quantum system formulation can be found in Appendix D and Ref. [77].

IV. QUANTUM ALGORITHM

To simulate the nonunitary evolution in Eq. (7) of the system on a quantum computer, we apply the Stinespring dilation theorem [19,88,104] to enlarge the Hilbert space, such that the system and additional ancillary qubits evolve unitarily together for small time steps. For the evolution from 0 to t, we divide the length of the time interval into N_{cycle} time steps or "cycles." For each cycle, we apply the algorithm with a time step $\Delta t = t/N_{\mathrm{cycle}}$ and the ancilla qubits are reset after each cycle. With qubit reset operations, we only need one ancilla qubit since Eq. (7) has only one Lindblad operator. The quantum algorithm is shown schematically in Fig. 2 for two cycles. The initial state is given by $|\psi_S(0)\rangle \otimes |0\rangle_a$, where the initial state of the Schwinger model $|\psi_S(0)\rangle$ is chosen to be the unoccupied bare vacuum state while the ancilla is initialized in the $|0\rangle$ state. The J operator is a 2×2 block matrix

$$J = \begin{pmatrix} 0 & L^\dagger \\ L & 0 \end{pmatrix}. \tag{10}$$

Other algorithms to simulate Lindblad equations are discussed in Refs. [64,88,105–110].

FIG. 2.   Quantum algorithm to simulate the time evolution governed by the Lindblad equation using the Stinespring dilation theorem [104] for two cycles with time step Δt. The two unitary operators are given by $U_J = \exp(-iJ\sqrt{\Delta t})$ and $U_{H_S} = \exp(-iH_S\Delta t)$. The ancilla qubit is reset after each cycle.

V. SIMULATION ON IBMQ

With the quantum algorithm discussed above, we begin by performing (noiseless) simulations using the IBMQ QISKIT simulator [111]. We count all units in terms of a and choose $e = 1/a$, $m = 0.1/a$ and $\beta \equiv 1/T = 0.1a$. We then set $a = 1$ and evolve in small time steps with $N_{\text{cycle}} = 200$. The results for two spatial lattice sites are shown in Fig. 3. We present results for both the expectation values of the number operators for e^+e^- pairs, $\langle N_{e^+e^-}\rangle$ (left), and of the electric flux $\langle E^2\rangle$ (right) as a function of time for two different values of the correlator D. The result for the closed quantum system is shown for comparison. The open system starts to rapidly deviate from the closed system and eventually approaches the thermal equilibrium. Due to the interactions with the environment, the oscillations are damped. Both the oscillation damping rate and the system thermalization rate depend on the value of D. The results of the quantum algorithm are consistent with the results obtained with a fourth order Runge-Kutta (RK4) method that solves Eq. (7) classically. In Appendix F, we show simulation results of our quantum circuit up to $N = 4$, which demonstrate similar agreement.

Next, we perform simulations using quantum devices from the IBMQ platform. We choose $N = 2$ spatial lattice sites, which requires 2 qubits to represent the system and 1

additional qubit to simulate the interaction with the environment. We apply measurement error corrections using IBM's QISKIT-IGNIS package [111]. In addition, we correct for the Controlled NOT (CNOT) gate errors using the zero-noise extrapolation of Ref. [112]. To minimize error corrections, we opt for using a different ancilla qubit for every cycle instead of resetting a single ancilla qubit [113]. We use the QSEARCH compiler of Ref. [114] to efficiently map the two unitary operators U_J and U_{H_S}, see Fig. 2, to the basis gate set of IBMQ which consists of the single-qubit rotations RZ, SX and X and the CNOT gate. One cycle (see Fig. 2) consists of 7–13 CNOT gates and ~100 single-qubit gates. We show the results from the IBMQ device IBMQ_MONTREAL [115] in Fig. 4, where we use a larger number of cycles (up to $N_{\text{cycle}} = 4$) as t increases. We find a very good agreement between the quantum device and the noiseless circuit simulator. The measurement error correction and the CNOT gate error mitigation mildly improve the agreement, and generally have a small impact. The performance deteriorates only slightly at later times due to the large number of CNOT gates. In addition, we observe that the quantum algorithm with four cycles gives a good approximation of the full result (labeled as "RK4 open system") up to $t \approx 6$. We are thus able to approximately prepare a thermal state of the Schwinger model from nonequilibrium dynamics. These results constitute the first studies of quantum simulations of quantum field theoretical nonequilibrium dynamics and thermalization.

In order for these simulations to describe physical systems, one needs to extrapolate to the infinite volume and continuum limits. As a first step, in Fig. 5, we investigate finite volume effects of our results by simulating lattices with a different number of spatial sites N, for fixed lattice spacing a. We plot the average electric field $\langle E^2\rangle$ using numerical methods (RK4) up to $N = 8$, and find the numerical solutions begin to converge as $N \to 8$.

FIG. 3.   Quantum simulation of nonequilibrium dynamics in the Schwinger model: $\langle N_{e^+e^-}\rangle$ (left) and $\langle E^2\rangle$ (right) using the quantum circuit in Fig. 2 for two spatial lattice sites with $N_{\text{cycle}} = 200$, $\beta = 0.1a$, $e = 1/a$, $m = 0.1/a$, $a = 1$ and different system-environment couplings. The time t is in units of a. For comparison, we also show a numerical solution (RK4) and the dotted line indicates the thermal equilibrium.
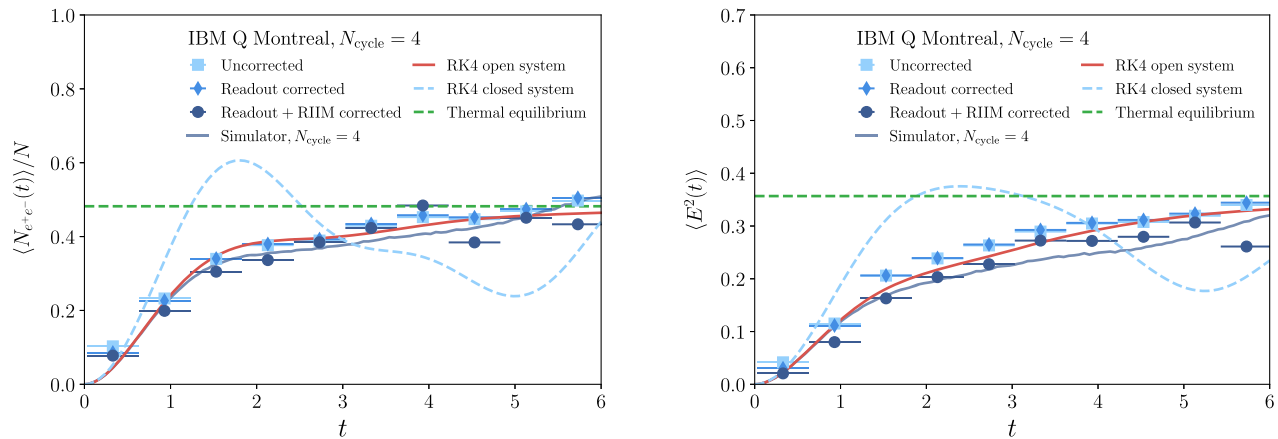
FIG. 4.   Results from the IBMQ_MONTREAL device [115] for $\langle N_{e^+e^-} \rangle$ (left) and $\langle E^2 \rangle$ (right) for $N = 2$ and $D = 3.2$ with up to four cycles, see Fig. 2. We include readout and CNOT error mitigation techniques as described in the text.
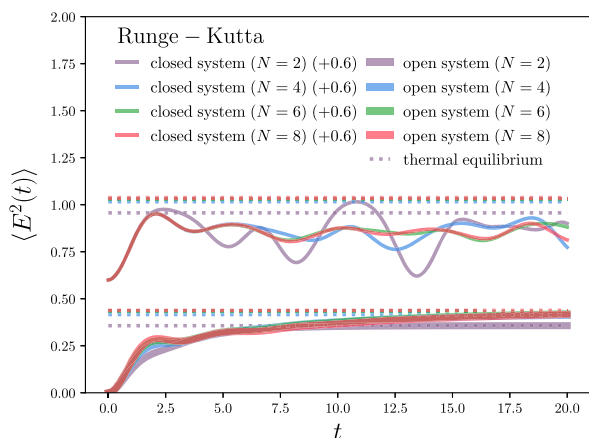

FIG. 5.   Numerical solution of nonequilibrium dynamics in the Schwinger model: $\langle E^2 \rangle$ up to $N = 8$ with $D = 3.2$.

As indicated by the dashed horizontal lines, we find a mild dependence of the thermal equilibrium values on N. Similar results for the number of electron-positron pairs are included in Appendix G. In order to make the extrapolated results stable at higher temperatures, one needs to consider larger values of N and include states with higher electric fluxes, since these states can then be excited more frequently. For such high temperatures and large values of N, it will be eventually essential to use quantum computers to simulate the dynamics due to the exponential growth of the size of the physical Hilbert space.

VI. CONCLUSIONS

We performed first quantum simulations of field-theoretical nonequilibrium dynamics of open quantum systems. We considered the Schwinger model discretized on a spatial lattice which interacts with a thermal scalar field theory. In the quantum Brownian motion limit, we derived the corresponding Lindblad evolution equation

which can be cast in the form of a field-theoretical Caldeira-Leggett equation. We computed the nonunitary Lindblad evolution with the IBM's simulator and quantum hardware. We employed suitable optimization algorithms and error mitigation techniques and found good agreement with the Runge-Kutta solution which sets a benchmark for future studies. In addition, we demonstrated a method for preparing thermal states for quantum computations of field theories—a step that is important for studies of systems at finite temperature. This work constitutes a starting point for simulations of the real-time evolution of nonequilibrium dynamics of quantum field theories with the ultimate goal of studying non-Abelian gauge theories in higher spatial dimensions.

APPENDIX A: HAMILTONIAN FORMULATION OF THE SCHWINGER MODEL IN THE CONTINUUM

The Lagrangian density of the (massive) Schwinger model is given by

$$\mathcal{L} = \bar{\psi}(i\slashed{D} - m)\psi - \frac{1}{4}F^{\mu\nu}F_{\mu\nu}, \tag{A1}$$

with $\slashed{D} = D_\mu \gamma^\mu$ and $\{\gamma^\mu, \gamma^\nu\} = 2g^{\mu\nu}$ for $\mu = 0, 1$. We use the metric that has $g^{00} = 1$ and $g^{11} = -1$. The covariant derivative is $D_\mu = \partial_\mu - ieA_\mu$. The gamma matrices in $1 + 1$ dimension can be chosen as

$$\gamma^0 = \sigma_z, \qquad \gamma^1 = i\sigma_y, \qquad \gamma^0\gamma^1 = \sigma_x, \tag{A2}$$

where $\sigma_{x,y,z}$ are the Pauli matrices. The electromagnetic field strength tensor is $F_{\mu\nu} = \partial_\mu A_\nu - \partial_\nu A_\mu$. In $1 + 1$ dimensions, the fermion field has two components: $\psi = (\psi_u, \psi_d)^T$. The mass dimensions of the fields and coupling constants are given by $[\psi] = [\bar{\psi}] = \frac{1}{2}$, $[A] = 0$, $[e] = 1$. The equation of motion associated with the gauge field A_0 is given by

$$0 = \frac{\partial\mathcal{L}}{\partial A_0} - \partial_1\frac{\partial\mathcal{L}}{\partial(\partial_1 A_0)} = e\bar{\psi}\gamma^0\psi + \partial_1 F^{10} = e\psi^\dagger\psi + \partial_1 E, \tag{A3}$$

which corresponds to Gauss's law and $E = F^{10}$ denotes the electric field.

For the Hamiltonian formulation of the Schwinger model, we will work in the axial gauge $A_0 = 0$. We denote the spatial component of the gauge field by $A_1 = -A^1 = A$ and we write the field strength tensor as $F^{10} = -F^{01} = E = \partial^0 A$. The canonical momenta Π_ψ and Π_A associated with the fermion and gauge fields, respectively, can be written as

$$\Pi_\psi = \frac{\partial\mathcal{L}}{\partial(\partial^0\psi)} = \bar{\psi}i\gamma^0 = i\psi^\dagger, \tag{A4}$$

$$\Pi_A = \frac{\partial\mathcal{L}}{\partial(\partial^0 A^1)} = -E. \tag{A5}$$

The nontrivial (anti)commutation relations from canonical quantization are given by

$$\{\psi(t,x), \Pi_\psi(t,y)\} = i\{\psi(t,x), \psi^\dagger(t,y)\} = i\delta(x-y), \tag{A6}$$

$$[A^1(t,x), \Pi_A(t,y)] = [A(t,x), E(t,y)] = i\delta(x-y). \tag{A7}$$

The Hamiltonian density is then given by

$$\begin{aligned}
\mathcal{H} &= \Pi_\psi \partial^0\psi + \Pi_A \partial^0 A^1 - \mathcal{L} \\
&= -i\bar{\psi}\gamma^1(\partial_1 + ieA^1)\psi + m\bar{\psi}\psi + \frac{1}{2}E^2.
\end{aligned} \tag{A8}$$

From now on, we will assume that all fields are in the Schrödinger picture. We note that in the Hamiltonian approach, Gauss's law is not generated by the equations of motion. Therefore, we have to impose $e\psi^\dagger\psi = -\partial_1 E$ when we construct the physical Hilbert space below.

For later convenience, we introduce the spatial Wilson line, the gauge link, as

$$\begin{aligned}
U(z,y) &= \mathcal{P}\exp\left(-ie\int_y^z dx\, A^1(x)\right) \\
&= \mathcal{P}\exp\left(ie\int_y^z dx\, A_1(x)\right), \\
&= \sum_{n=0}^\infty \frac{(ie)^n}{n!}\int_y^z dx_1\int_y^z dx_2\cdots \\
&\quad \times \int_y^z dx_n \mathcal{P}(A_1(x_1)A_1(x_2)\cdots A_1(x_n)), \tag{A9}
\end{aligned}$$

where $\mathcal{P}$ denotes the path ordering operator. Using $[E(x), A_1(y)] = -i\delta(x-y)$ and

$$\begin{aligned}
&[E(y), \mathcal{P}(A_1(x_1)A_1(x_2)\cdots A_1(x_n))] \\
&= -i\delta(y-x_1)\mathcal{P}(A_1(x_2)A_1(x_3)\cdots A_1(x_n)) \\
&\quad - i\delta(y-x_2)\mathcal{P}(A_1(x_1)A_1(x_3)A_1(x_4)\cdots A_1(x_n)) \\
&\quad - \cdots \\
&\quad - i\delta(y-x_n)\mathcal{P}(A_1(x_1)A_1(x_2)\cdots A_1(x_{n-1})), \tag{A10}
\end{aligned}$$

we find

$$[E(y), U(z,y)] = eU(z,y). \tag{A11}$$

APPENDIX B: LATTICE DISCRETIZATION

We now review the lattice discretization of the Hamiltonian of the Schwinger model. We consider a one-dimensional spatial lattice with lattice spacing a, while keeping time continuous. We label the lattice sites with an integer n starting from $n = 0$. The fields $\psi(x)$ and $A(x)$ at position $x = na$ are then labeled as $\psi(n)$ and $A(n)$, respectively. The discretized version of the fermionic part of the Hamiltonian $H_f = \int dx\, \mathcal{H}_f(x)$ can be written as

$$H_f = a \sum_n \left(-i\bar{\psi}(n)\gamma^1 \frac{\psi(n+1)-\psi(n-1)}{2a} + m\bar{\psi}(n)\psi(n) + e\bar{\psi}(n)\gamma^1 A^1(n)\frac{\psi(n+1)+\psi(n-1)}{2} \right) + \mathcal{O}(a^3),$$

$$= a \sum_n \left(-i\psi^\dagger(n)\sigma_x \frac{\psi(n+1)-\psi(n-1)}{2a} + m\psi^\dagger(n)\sigma_z\psi(n) - e\psi^\dagger(n)\sigma_x A(n)\frac{\psi(n+1)+\psi(n-1)}{2} \right) + \mathcal{O}(a^3), \quad \text{(B1)}$$

where we have used $A^1 = -A$. To put the two-component fermion field $\psi = (\psi_u, \psi_d)^T$ on a lattice, we use the Kogut-Susskind staggered fermion approach [31,97,98], where a field $\chi(n)$ with mass dimension 0 is introduced as[1]

$$\chi(n) = \sqrt{a}(\sigma_x)^n\psi(n), \qquad \chi^\dagger(n) = \sqrt{a}\psi^\dagger(n)(\sigma_x)^n. \quad \text{(B2)}$$

The Hamiltonian can then be written as

$$H_f = \frac{1}{2a}\sum_n (-i\chi^\dagger(n)\chi(n+1) - ae\chi^\dagger(n)A(n)\chi(n+1)$$
$$+ i\chi^\dagger(n)\chi(n-1) - ae\chi^\dagger(n)A(n)\chi(n-1)$$
$$+ 2ma(-1)^n\chi^\dagger(n)\sigma_z\chi(n) + \mathcal{O}(a^2)), \quad \text{(B3)}$$

where we have used $\sigma_x^2 = 1$. Using the definition of the gauge link in Eq. (A9), we can write

$$\chi^\dagger(n)U(n,n+1)\chi(n+1)$$
$$= \chi^\dagger(n)\mathcal{P}e^{ie\int_{(n+1)a}^{na} dx A(x)}\chi(n+1),$$
$$= \chi^\dagger(n)\chi(n+1) - iae\chi^\dagger(n)A(n)\chi(n+1)$$
$$+ \mathcal{O}(a^2), \quad \text{(B4)}$$

and similarly

$$\chi^\dagger(n)U(n,n-1)\chi(n-1)$$
$$= \chi^\dagger(n)\chi(n-1) + iae\chi^\dagger(n)A(n)\chi(n-1) + \mathcal{O}(a^2). \quad \text{(B5)}$$

Then we can write the Hamiltonian as

$$H_f = \frac{1}{2a}\sum_n (-i\chi^\dagger(n)U(n,n+1)\chi(n+1) + i\chi^\dagger(n)U(n,n-1)\chi(n-1) + 2ma(-1)^n\chi^\dagger(n)\sigma_z\chi(n)),$$

$$= \frac{1}{2a}\sum_n (-i\chi_u^\dagger(n)U(n,n+1)\chi_u(n+1) + i\chi_u^\dagger(n)U(n,n-1)\chi_u(n-1) + 2ma(-1)^n\chi_u^\dagger(n)\chi_u(n)$$

$$- i\chi_d^\dagger(n)U(n,n+1)\chi_d(n+1) + i\chi_d^\dagger(n)U(n,n-1)\chi_d(n-1) - 2ma(-1)^n\chi_d^\dagger(n)\chi_d(n)). \quad \text{(B6)}$$

where in the last two lines we have explicitly written out the upper and lower components of the fermion field χ. We note that the lower component ψ_d at odd (even) sites behaves in the same way as the upper component ψ_u at even (odd) sites. Therefore, we can discard the lower component ψ_d and treat the field χ in the first line of Eq. (B6) as a single-component, Grassmann-valued field. The summation here is over N_f fermion sites with spacing a and two fermion sites per spatial lattice site as illustrated in Fig. 1.

Next, we apply the Jordan-Wigner transformation [99] which maps the staggered fermion fields to spin matrices as

$$\chi_u(n) \to \left(\prod_{m<n} - i\sigma_z(m)\right)\sigma^-(n),$$
$$\chi_u^\dagger(n) \to \sigma^+(n)\left(\prod_{m<n} + i\sigma_z(m)\right), \quad \text{(B7)}$$

where we define $\sigma^\pm(n) = (\sigma_x(n) \pm i\sigma_y(n))/2$ as the ladder matrices at site n. To complete the lattice formulation of the Schwinger model, we also need to discretize the electric field and the gauge link. There are different approaches in the literature to treat the infinite dimensional Hilbert space of the gauge field. The so-called quantum link model [36–39] replaces U(1) gauge fields by spin variables, which allows for finite, but nonunitary representations of the canonical commutation relations. In Refs. [40,41], the gauge field is eliminated using Gauss's law at the cost of long-range interactions. In Refs. [42,46], the U(1) gauge degrees of freedom are described by the finite dimensional implementation through the discrete group $\mathbb{Z}_m$, where U(1) is restored in the large-m limit. In our work, we follow the approach of Ref. [43]. The Hilbert space is restricted to physical

---

[1]An alternative definition of $\chi(n)$ is

$$\begin{cases} \frac{\chi(2n)}{\sqrt{a}} = \psi_u(n) \\ \frac{\chi(2n+1)}{\sqrt{a}} = \psi_d(n) \end{cases}.$$

In either definition of $\chi(n)$, the number of fermion lattice sites required to represent $N_f/2$ spatial sites is N_f.

states which satisfy Gauss's law and an upper cutoff on the Hilbert space of the gauge field is imposed. The discretized version of the commutation relation in Eq. (A11) can be written as

$$[E(n), U(n+1, n)] = eU(n+1, n). \tag{B8}$$

This quantum system for each n can be solved like a harmonic oscillator:

$$E(n)|\ell_n\rangle = e\ell_n|\ell_n\rangle, \tag{B9}$$

$$U(n \pm 1, n)|\ell_n\rangle = |\ell_n \pm 1\rangle. \tag{B10}$$

Here $\ell_n = 0, \pm 1, \pm 2, \ldots$ denotes the eigenvalue (up to the factor e) of the electric operator $E(n)$ at site n and $|\ell_n\rangle$ denotes the corresponding eigenstate. Using the eigenstates as a basis, the electric field and the gauge link can be represented as

$$E(n) \to e\ell_n, \quad U(n, n-1) \to L_{n-1}^+, \quad U(n, n+1) \to L_n^- \tag{B11}$$

The $L_n^\pm$ operators raise/lower the electric flux on the link between the fermion sites n and $n+1$ and act as $L_n^\pm|\ell_n\rangle = |\ell_n \pm 1\rangle$. Putting everything together, we finally obtain the discretized Hamiltonian of the Schwinger model

$$H_S = \frac{1}{2a}\sum_n (\sigma^+(n)L_n^-\sigma^-(n+1) + \sigma^+(n)L_{n-1}^+\sigma^-(n-1))$$
$$+ \frac{m}{2}\sum_n (-1)^n(\sigma_z(n) + 1) + \frac{ae^2}{2}\sum_n \ell_n^2. \tag{B12}$$

We employ periodic boundary conditions such that the one-dimensional chain shown in Fig. 1 effectively forms a circle. Note that in the main text, we redefine n by $n+1$ for the second term in the Hamiltonian. As discussed earlier, Gauss's law $\partial_1 E = -e\psi^\dagger\psi$ has to be imposed to form physical states, which has the discrete form:

$$E(n+1) - E(n) = -e\sigma^+(n)\sigma^-(n) - e\frac{(-1)^n - 1}{2}, \tag{B13}$$

where the constant term appears in the staggered fermion approach. Imposing Gauss's law significantly reduces the size of the Hilbert space, though the size of the Hilbert space of physical states still grows exponentially with the number of lattice sites. In fact, we find an analytical expression for the number of physical states, which will be discussed further below.

For our numerical calculations, we project onto states with zero momentum $\mathbf{k} = 0$ and positive parity. The zero-momentum states can be constructed by first defining equivalent classes under cyclic permutations. In each equivalent class, the states are related to each other via cyclic permutations. Then the symmetrized linear combination of all states in the same equivalent class gives one zero-momentum state. The parity transformation is defined by a reflection with respect to a given site. If a zero-momentum state is invariant under the parity transformation, then it is a positive parity state itself. If a zero-momentum state becomes another zero-momentum state under the parity transformation, then their symmetrized linear combination gives a positive parity state. We have set up a PYTHON code that can generate all the physical states, project onto the states with zero-momentum and positive parity and compute the corresponding Hamiltonian matrix in the basis of these states. We verified the result of our code by an explicit calculation for $N = 2, 4$ spatial lattice sites.

With a cutoff $|\ell_n| \leq 1$ on the quantized electric flux, the Hamiltonian for two spatial lattice sites can be written as [43]

$$H_S^{\mathbf{k}=\mathbf{0},+} = \begin{pmatrix} -2m & \frac{1}{a} & 0 & 0 & 0 \\ \frac{1}{a} & \frac{ae^2}{2} & \frac{1}{\sqrt{2a}} & 0 & 0 \\ 0 & \frac{1}{\sqrt{2a}} & ae^2 + 2m & \frac{1}{\sqrt{2a}} & 0 \\ 0 & 0 & \frac{1}{\sqrt{2a}} & \frac{3ae^2}{2} & \frac{1}{\sqrt{2a}} \\ 0 & 0 & 0 & \frac{1}{\sqrt{2a}} & 2ae^2 - 2m \end{pmatrix}. \tag{B14}$$

For four spatial lattice sites we have

$H_S^{\mathbf{k}=\mathbf{0},+}$

$$
=\begin{pmatrix}
-4m & \frac{\sqrt{2}}{a} & 0 & 0 & 0 & 0 & 0 & 0 & 0 & 0 & 0 & 0 & 0 & 0 & 0 & 0 & 0 & 0 & 0 \\
\frac{\sqrt{2}}{a} & \frac{ae^2}{2}-2m & \frac{1}{a} & \frac{1}{\sqrt{2}a} & \frac{1}{\sqrt{2}a} & \frac{1}{\sqrt{2}a} & 0 & 0 & 0 & 0 & 0 & 0 & 0 & 0 & 0 & 0 & 0 & 0 & 0 \\
0 & \frac{1}{a} & ae^2 & 0 & 0 & 0 & \frac{1}{2a} & \frac{1}{a} & \frac{1}{2a} & 0 & 0 & 0 & 0 & 0 & 0 & 0 & 0 & 0 & 0 \\
0 & \frac{1}{\sqrt{2}a} & 0 & ae^2 & 0 & 0 & 0 & 0 & \frac{1}{\sqrt{2}a} & 0 & 0 & 0 & 0 & 0 & 0 & 0 & 0 & 0 & 0 \\
0 & \frac{1}{\sqrt{2}a} & 0 & 0 & ae^2 & 0 & 0 & \frac{1}{\sqrt{2}a} & 0 & 0 & 0 & 0 & 0 & 0 & 0 & 0 & 0 & 0 & 0 \\
0 & \frac{1}{\sqrt{2}a} & 0 & 0 & 0 & ae^2 & 0 & 0 & \frac{1}{\sqrt{2}a} & 0 & 0 & 0 & 0 & 0 & 0 & 0 & 0 & 0 & 0 \\
0 & 0 & \frac{1}{2a} & 0 & 0 & 0 & \frac{3}{2}ae^2-2m & 0 & 0 & \frac{1}{2a} & \frac{1}{2a} & \frac{1}{2a} & 0 & 0 & 0 & 0 & 0 & 0 & 0 \\
0 & 0 & \frac{1}{a} & 0 & \frac{1}{\sqrt{2}a} & 0 & 0 & \frac{3}{2}ae^2+2m & 0 & \frac{1}{2a} & 0 & \frac{1}{2a} & \frac{1}{a} & 0 & 0 & 0 & 0 & 0 & 0 \\
0 & 0 & \frac{1}{2a} & \frac{1}{\sqrt{2}a} & 0 & \frac{1}{\sqrt{2}a} & 0 & 0 & \frac{3}{2}ae^2+2m & 0 & \frac{1}{2a} & 0 & 0 & 0 & 0 & 0 & 0 & 0 & 0 \\
0 & 0 & 0 & 0 & 0 & 0 & \frac{1}{2a} & \frac{1}{2a} & 0 & 2ae^2 & 0 & 0 & 0 & \frac{1}{2a} & \frac{1}{2a} & 0 & 0 & 0 & 0 \\
0 & 0 & 0 & 0 & 0 & 0 & \frac{1}{2a} & 0 & \frac{1}{2a} & 0 & 2ae^2 & 0 & 0 & 0 & 0 & 0 & 0 & 0 & 0 \\
0 & 0 & 0 & 0 & 0 & 0 & \frac{1}{2a} & \frac{1}{2a} & 0 & 0 & 0 & 2ae^2 & 0 & \frac{1}{2a} & \frac{1}{2a} & 0 & 0 & 0 & 0 \\
0 & 0 & 0 & 0 & 0 & 0 & 0 & \frac{1}{a} & 0 & 0 & 0 & 0 & 2ae^2+4m & 0 & \frac{1}{a} & 0 & 0 & 0 & 0 \\
0 & 0 & 0 & 0 & 0 & 0 & 0 & 0 & 0 & \frac{1}{2a} & 0 & \frac{1}{2a} & 0 & \frac{5}{2}ae^2-2m & 0 & \frac{1}{2a} & 0 & 0 & 0 \\
0 & 0 & 0 & 0 & 0 & 0 & 0 & 0 & 0 & \frac{1}{2a} & 0 & \frac{1}{2a} & \frac{1}{a} & 0 & \frac{5}{2}ae^2+2m & \frac{1}{a} & \frac{1}{\sqrt{2}a} & 0 & 0 \\
0 & 0 & 0 & 0 & 0 & 0 & 0 & 0 & 0 & 0 & 0 & 0 & 0 & \frac{1}{2a} & \frac{1}{a} & 3ae^2 & 0 & \frac{1}{a} & 0 \\
0 & 0 & 0 & 0 & 0 & 0 & 0 & 0 & 0 & 0 & 0 & 0 & 0 & 0 & \frac{1}{\sqrt{2}a} & 0 & 3ae^2 & \frac{1}{\sqrt{2}a} & 0 \\
0 & 0 & 0 & 0 & 0 & 0 & 0 & 0 & 0 & 0 & 0 & 0 & 0 & 0 & 0 & \frac{1}{a} & \frac{1}{\sqrt{2}a} & \frac{7}{2}ae^2-2m & \frac{1}{a} \\
0 & 0 & 0 & 0 & 0 & 0 & 0 & 0 & 0 & 0 & 0 & 0 & 0 & 0 & 0 & 0 & 0 & \frac{1}{a} & 4ae^2-4m
\end{pmatrix}.
$$

$$(B15)$$

Here the states are arranged in ascending order in terms of gauge fields and e^+e^- pairs. We note that we find full agreement when comparing the ground state energy eigenvalues to the results given in Ref. [43]. For completeness, we also give the measurement operators $\hat{A}$ for the electric field and the number of e^+e^- pairs in this basis, which are defined by

$$\hat{A}_{E^2} = \frac{1}{2Na}\int \mathrm{d}x\, E^2(x) = \frac{e^2}{2N}\sum_n \ell_n^2, \qquad (B16)$$

$$\hat{A}_{N_{e^+e^-}} = \sum_{n,\text{even}} \sigma^+(n)\sigma^-(n), \qquad (B17)$$

respectively, where $2Na = aN_f$ is the total length of the spatial lattice. Here even lattice sites correspond to electrons. For two spatial lattice sites we find

$$\hat{A}_{E^2}^{\mathbf{k}=\mathbf{0},+} = \frac{e^2}{4}\mathrm{diag}(0,1,2,3,4), \qquad (B18)$$

$$\hat{A}_{N_{e^+e^-}}^{\mathbf{k}=\mathbf{0},+} = \mathrm{diag}(0,1,2,1,0), \qquad (B19)$$

and for four spatial lattice sites we have

$$\hat{A}_{E^2}^{\mathbf{k}=\mathbf{0},+} = \frac{e^2}{8}\mathrm{diag}(0,1,2,2,2,2,3,3,3,4,4,4,4,$$
$$5,5,6,6,7,8), \qquad (B20)$$

$$\hat{A}_{N_{e^+e^-}}^{\mathbf{k}=\mathbf{0},+} = \mathrm{diag}(0,1,2,2,2,2,1,3,3,2,2,2,4,1,3,2,2,1,0). \qquad (B21)$$

The observables that we study in the main text are defined by

$$\langle E^2(t)\rangle \equiv \mathrm{Tr}(\rho_S(t)\hat{A}_{E^2}), \qquad (B22)$$

$$\langle N_{e^+e^-}(t)\rangle \equiv \mathrm{Tr}(\rho_S(t)\hat{A}_{N_{e^+e^-}}). \qquad (B23)$$

APPENDIX C: COMBINATORICS OF THE SCHWINGER MODEL

In this section, we derive the combinatorial formula in Eq. (3) which counts the number of physical states satisfying Gauss's law for a given lattice size. We take the size of the spatial lattice to be N, which means there are N electron and N positron sites. We impose a cutoff on the electric flux at each link, i.e. $|\ell_n| \leq 1$ for $n = 0, 1, \ldots, 2N-1$. Then the number of physical states with M pairs of e^+e^-, denoted by $D_{N,M}$, is given by, up to a symmetry factor that will

be described below, the number of unique solutions $(x_1, x_2, \ldots, x_M; y_1, y_2, \ldots, y_M)$ of the partition equation

$$x_1 + x_2 + \cdots + x_M + y_1 + y_2 + \cdots + y_M = 2N, \quad \text{(C1)}$$

where $x_i \in \{1, 3, 5, \ldots\}$ and $y_i \in \{1, 2, 3, 4, \ldots\}$. Here, x_i represents the distance between the ith $e^+ e^-$ pair connected by an electric field, which is always an odd integer. Moreover, y_i represents the size of the ith gap between different fermions where the electric flux is zero. The length of these gaps is always a positive integer. Using the "stars-and-bars" method in combinatorics [116] to solve Eq. (C1) and including the symmetry factor $2N/M$, we arrive at

$$D_{N,M} = \frac{2N}{M} \sum_{K=0}^{N-M} \binom{M-1+K}{M-1} \binom{2N-2K-M-1}{M-1},$$
$$\text{for } M = 1, 2, \ldots, N. \quad \text{(C2)}$$

The $2N$ of the overall symmetry factor $2N/M$ can be understood as the number of cyclic permutations that creates unique configurations. The $1/M$ is a factor to correct for overcounting since $(x_1, \ldots, x_M, y_1, \ldots, y_M) = (x_2, \ldots, x_M, x_1; y_2, \ldots, y_M, y_1) = \cdots = (x_M, x_1, \ldots, x_{M-1}; y_M, y_1, \ldots, y_{M-1})$ describe the same physical configuration. Finally, we arrive at the expression that gives the total number of physical configurations with the restriction $|\ell_n| \le 1$:

TABLE I.   Number of physical states in the Hilbert space of the Schwinger model D_N for $|\ell_n| \le 1$ up to $N = 100$ spatial lattice sites.

N	D_N
1	5
2	13
4	117
6	1,186
8	12,389
10	130,338
12	1,373,466
14	14,478,659
16	152,642,789
18	1,609,284,589
20	16,966,465,802
⋮	⋮
50	37,495,403,206,807,318,414,369,013
⋮	⋮
100	1,405,905,261,641,056,248,331,375,526, 910,312,847,554,957,270,229,877

$$D_N \equiv \sum_{M=1}^{N} D_{N,M} + D_{N,0},$$
$$= \sum_{M=1}^{N} \frac{2N}{M} \sum_{K=0}^{N-M} \binom{M-1+K}{M-1} \binom{2N-2K-M-1}{M-1} + 3. \quad \text{(C3)}$$

We note that $D_{N,0} = 3$ for all N, which counts the states with no $e^+ e^-$ pairs and the electric flux is everywhere -1 or 0 or 1.

With this closed formula, we give results of D_N explicitly for different values of N in Table 1. We find agreement with Ref. [43] where the results up to $N = 12$ were given.

APPENDIX D: OPEN QUANTUM SYSTEMS, LINDBLAD EVOLUTION AND QUANTUM BROWNIAN MOTION

We consider the Schwinger model coupled to a thermal scalar field. The Hamiltonian of the whole system, which consists of the system (the Schwinger model) and the environment (the thermal scalar field), can be written as

$$H = H_S + H_E + H_I. \quad \text{(D1)}$$

Here H_S and H_E denote the Hamiltonians of the system and the environment, respectively. The Hamiltonian of the $(1 + 1)$-dimensional scalar field can be written as

$$H_E = \int dx \left[\frac{1}{2} \Pi^2 + \frac{1}{2} (\nabla \phi)^2 + \frac{1}{2} m_\phi^2 \phi^2 + \frac{1}{4!} g \phi^4 \right], \quad \text{(D2)}$$

where Π is the canonical momentum conjugate to ϕ and $g > 0$. The interaction Hamiltonian is assumed to be a Yukawa-type coupling:

$$H_I = \lambda \int dx \, \phi(x) \bar{\psi}(x) \psi(x) = \int dx \, O_E(x) O_S(x), \quad \text{(D3)}$$

where $O_E(x) = \lambda \phi(x)$ and $O_S(x) = \bar{\psi}(x) \psi(x)$. The time evolution of the whole system is given by the von Neumann equation

$$\frac{d\rho(t)}{dt} = -i[H, \rho(t)]. \quad \text{(D4)}$$

Tracing out the environment degrees of freedom, we obtain the reduced evolution equation of the system (the Schwinger model) in the interaction picture

$$\rho_S^{(\text{int})}(t) = \text{Tr}_E(\rho^{(\text{int})}(t)) = \text{Tr}_E(U(t)\rho^{(\text{int})}(0)U^\dagger(t)), \quad \text{(D5)}$$

$$U(t) = \mathcal{T} \exp\left(-i \int_0^t H_I^{(\text{int})}(t') dt'\right). \quad \text{(D6)}$$

Here $\mathcal{T}$ denotes the time ordering operator. The density matrix and the interaction Hamiltonian in the interaction picture are defined by

$$\rho^{(\mathrm{int})}(t) = e^{i(H_S+H_E)t}\rho(t)e^{-i(H_S+H_E)t}, \quad \text{(D7)}$$

$$H_I^{(\mathrm{int})}(t) = e^{i(H_S+H_E)t}H_I e^{-i(H_S+H_E)t}$$
$$= \int \mathrm{d}x O_E^{(\mathrm{int})}(t,x)O_S^{(\mathrm{int})}(t,x), \quad \text{(D8)}$$

respectively, where $O_{E/S}^{(\mathrm{int})}(t,x) = e^{iH_{E/S}t}O_{E/S}(x)e^{-iH_{E/S}t}$. Since the environment scalar field is thermal, we have

$$\rho_E^{(\mathrm{int})}(t) = \rho_E = \frac{e^{-\beta H_E}}{\mathrm{Tr}_E e^{-\beta H_E}}, \quad \text{(D9)}$$

where $\beta = 1/T$ and T is the temperature of the environment. If we assume that the initial density matrix factorizes

$$\rho^{(\mathrm{int})}(t=0) = \rho_S^{(\mathrm{int})}(t=0) \otimes \rho_E, \quad \text{(D10)}$$

and that the interaction between the system and the environment is weak (the system and the environment themselves can be strongly coupled), we obtain by expanding the evolution operator to second order in $H_I^{(\mathrm{int})}$, the following result

$$\rho_S^{(\mathrm{int})}(t) = \rho_S^{(\mathrm{int})}(0) - \int_0^t \mathrm{d}t_1 \int_0^t \mathrm{d}t_2 \int \mathrm{d}x_1 \int \mathrm{d}x_2 \frac{\mathrm{sign}(t_1-t_2)}{2} D(t_1,x_1;t_2,x_2)[O_S^{(\mathrm{int})}(t_1,x_1)O_S^{(\mathrm{int})}(t_2,x_2),\rho_S^{(\mathrm{int})}(0)]$$
$$+ \int_0^t \mathrm{d}t_1 \int_0^t \mathrm{d}t_2 \int \mathrm{d}x_1 \int \mathrm{d}x_2 D(t_1,x_1;t_2,x_2)\left(O_S^{(\mathrm{int})}(t_2,x_2)\rho_S^{(\mathrm{int})}(0)O_S^{(\mathrm{int})}(t_1,x_1)\right.$$
$$\left. -\frac{1}{2}\{O_S^{(\mathrm{int})}(t_1,x_1)O_S^{(\mathrm{int})}(t_2,x_2),\rho_S^{(\mathrm{int})}(0)\}\right) + \mathcal{O}((tH_I^{(\mathrm{int})})^3). \quad \text{(D11)}$$

Here the environment correlator is defined as

$$D(t_1,x_1;t_2,x_2) = \mathrm{Tr}_E(\rho_E O_E^{(\mathrm{int})}(t_1,x_1)O_E^{(\mathrm{int})}(t_2,x_2)), \quad \text{(D12)}$$

and we have used $\mathrm{Tr}_E(\rho_E O_E^{(\mathrm{int})}(t,x)) = 0$, which can be realized by redefinitions of O_E and H_S [77].

The expression in Eq. (D11) is a finite-difference equation. It can be converted into a well-defined differential equation in the quantum Brownian motion limit. The limit of quantum Brownian motion is specified by the following separation of timescales:

$$\tau_R \gg \tau_E, \quad \text{(D13)}$$

$$\tau_S \gg \tau_E, \quad \text{(D14)}$$

where τ_R is the relaxation time of the system, τ_E denotes the environment correlation time and τ_S represents the intrinsic timescale of the system. The hierarchy $\tau_R \gg \tau_E$ leads to Markovian dynamics and is generally true when the interaction described by H_I is weak. The hierarchy $\tau_S \gg \tau_E$ is valid if $T \gg H_S$ since $\tau_E \sim 1/T$ and $\tau_S \sim 1/H_S$. Simplifying Eq. (D11) using these two hierarchies of timescales leads to the Schödinger-picture Lindblad equation in the limit of quantum Brownian motion (some higher order terms in the expansion of $\frac{\tau_E}{\tau_S}$ are included here. Details of the derivation can be found in Ref. [77]):

$$\frac{\mathrm{d}\rho_S(t)}{\mathrm{d}t} = -i[H_S + \Delta H_S, \rho_S(t)]$$
$$+ \int \mathrm{d}x_1 \mathrm{d}x_2 D(k_0=0,x_1-x_2)$$
$$\times \left(\tilde{O}_S(x_2)\rho_S(t)\tilde{O}_S^\dagger(x_1) - \frac{1}{2}\{\tilde{O}_S^\dagger(x_1)\tilde{O}_S(x_2),\rho_S(t)\}\right). \quad \text{(D15)}$$

Here ΔH_S denotes the correction to the system Hamiltonian due to the interaction with the environment and we have

$$\Delta H_S \equiv \frac{1}{2}\int \mathrm{d}x_1 \mathrm{d}x_2 \Sigma(k_0=0,x_1-x_2)O_S(x_1)O_S(x_2)$$
$$+ \frac{1}{4}\int \mathrm{d}x_1 \mathrm{d}x_2 \frac{\partial\Sigma(k_0=0,x_1-x_2)}{\partial k_0}$$
$$\times ([H_S,O_S(x_1)]O_S(x_2) - O_S(x_1)[H_S,O_S(x_2)]), \quad \text{(D16)}$$

$$\Sigma(k_0,x_1-x_2) \equiv -i\int \mathrm{d}(t_1-t_2)e^{ik_0(t_1-t_2)}\mathrm{sign}(t_1-t_2)$$
$$\times D(t_1,x_1;t_2,x_2), \quad \text{(D17)}$$

$$D(k_0,x_1-x_2) \equiv \int \mathrm{d}(t_1-t_2)e^{ik_0(t_1-t_2)}D(t_1,x_1;t_2,x_2), \quad \text{(D18)}$$

$$\tilde{O}_S(x) \equiv O_S(x) - \frac{1}{4T}[H_S, O_S(x)], \qquad \text{(D19)}$$

$$\tilde{O}_S^\dagger(x) \equiv O_S(x) + \frac{1}{4T}[H_S, O_S(x)]. \qquad \text{(D20)}$$

When defining the Fourier transform of the environment correlator in Eqs. (D17) and (D18), we have assumed that the environment is invariant under spacetime translations. We drop the correction to the system Hamiltonian ΔH_S in the main text since we want the equilibrium state of the evolution equation to be the thermal state of the Schwinger model in the vacuum. It is necessary to keep the

commutator terms in the definitions of $\tilde{O}_S$ and $\tilde{O}_S^\dagger$ for the system to thermalize (approximately).

For the Hilbert space of the zero-momentum states in the Schwinger model, considered in the main text, only the environment correlator $D(k_0 = 0, k = 0)$ contributes. To see this more explicitly, we sandwich Eq. (D15) with $\langle k=0,\alpha|$ and $|k=0,\beta\rangle$ and insert the identity $\sum_\alpha |k=0,\alpha\rangle \times \langle k=0,\alpha| = I$ (this is complete since we constrain the Hilbert space to include just the zero-momentum states) where the quantum numbers α and β label different zero-momentum states. Denoting $\langle k=0,\alpha|\rho_S(t)|k=0,\beta\rangle = \rho_S^{\alpha\beta}(t)$, $\langle k=0,\alpha|H_S|k=0,\beta\rangle = H_S^{\alpha\beta}$, and $\langle k=0,\alpha|\tilde{O}_S(x)|k=0,\beta\rangle = \tilde{O}_S^{\alpha\beta}(x)$, we obtain

$$\frac{d\rho_S^{\alpha\beta}(t)}{dt} = -i\sum_\gamma (H_S^{\alpha\gamma}\rho_S^{\gamma\beta}(t) - \rho_S^{\alpha\gamma}(t)H_S^{\gamma\beta}) + \int dx_1 dx_2 D(k_0 = 0, x_1 - x_2)$$
$$\times \left(\tilde{O}_S^{\alpha\gamma}(x_2)\rho_S^{\gamma\delta}(t)\tilde{O}_S^{\dagger\delta\beta}(x_1) - \frac{1}{2}\tilde{O}_S^{\dagger\alpha\gamma}(x_1)\tilde{O}_S^{\gamma\delta}(x_2)\rho_S^{\delta\beta}(t) - \frac{1}{2}\rho_S^{\alpha\gamma}(t)\tilde{O}_S^{\dagger\gamma\delta}(x_1)\tilde{O}_S^{\delta\beta}(x_2) \right). \qquad \text{(D21)}$$

Since the basis states have zero momentum, the projection of the system operator $O_S(x)$,

$$\langle k=0,\alpha|\tilde{O}_S(x)|k=0,\beta\rangle = \langle k=0,\alpha|e^{-i\hat{p}x}\tilde{O}_S(x=0)e^{i\hat{p}x}|k=0,\beta\rangle = \langle k=0,\alpha|\tilde{O}_S(x=0)|k=0,\beta\rangle$$
$$= \frac{1}{2Na}\int dx \langle k=0,\alpha|\tilde{O}_S(x)|k=0,\beta\rangle \qquad \text{(D22)}$$

is independent of the position x, where $\hat{p}$ is the momentum operator. Therefore, we can drop the dependence on x_1 and x_2 of the operators $\tilde{O}_S$ and $\tilde{O}_S^\dagger$, and we obtain

$$\frac{d\rho_S^{\alpha\beta}(t)}{dt} = -i\sum_\gamma (H_S^{\alpha\gamma}\rho_S^{\gamma\beta}(t) - \rho_S^{\alpha\gamma}(t)H_S^{\gamma\beta}) + \int dx D(k_0 = 0, k = 0)$$
$$\times \left(\tilde{O}_S^{\alpha\gamma}\rho_S^{\gamma\delta}(t)\tilde{O}_S^{\dagger\delta\beta} - \frac{1}{2}\tilde{O}_S^{\dagger\alpha\gamma}\tilde{O}_S^{\gamma\delta}\rho_S^{\delta\beta}(t) - \frac{1}{2}\rho_S^{\alpha\gamma}(t)\tilde{O}_S^{\dagger\gamma\delta}\tilde{O}_S^{\delta\beta} \right). \qquad \text{(D23)}$$

Here $\int dx D(k_0 = 0, k = 0)$ is independent of the position. Different values of the environment correlator $D(k_0 = 0, k = 0)$ will only modify the rate at which the system approaches equilibrium. The equilibrium properties of the system are independent of $D(k_0 = 0, k = 0)$. Therefore, we will take the constant $D(k_0 = 0, k = 0)$ as an input parameter in our calculations. The mass dimension of $D(k_0 = 0, k = 0)$ is 0. The matrix representation of the system operator $O_S^{\alpha\beta}$ in the discretized Schwinger model can be written as

$$O_S^{\alpha\beta} = \frac{1}{aN_f}\int dx \langle k=0,\alpha|\tilde{O}_S(x)|k=0,\beta\rangle = \frac{1}{aN_f}\int dx \langle k=0,\alpha|\bar{\psi}\psi(x)|k=0,\beta\rangle,$$
$$= \frac{1}{aN_f}\sum_n \langle k=0,\alpha|(-1)^n\bar{\chi}\chi(n)|k=0,\beta\rangle,$$
$$= \frac{1}{aN_f}\sum_n \langle k=0,\alpha|(-1)^n(\bar{\chi}_u\chi_u(n) + \bar{\chi}_d\chi_d(n))|k=0,\beta\rangle,$$
$$= \frac{1}{aN_f}\sum_n \langle k=0,\alpha|\frac{(-1)^n(\sigma_z(n)+1)}{2}|k=0,\beta\rangle, \qquad \text{(D24)}$$

where we have dropped the lower component χ_d as before. Defining the Lindblad operator as

$$L = \sqrt{aN_f D(k_0 = 0, k = 0)}\left(O_S - \frac{1}{4T}[H_S, O_S]\right), \quad \text{(D25)}$$

we can rewrite the Lindblad equation in Eq. (D23) in the form

$$\frac{d\rho_S(t)}{dt} = -i[H_S, \rho_S(t)] + L\rho_S(t)L^\dagger - \frac{1}{2}\{L^\dagger L, \rho_S(t)\}, \quad \text{(D26)}$$

where we have omitted the matrix indices.

APPENDIX E: IMPLEMENTATION ON IBMQ

In order to simulate the Lindblad equation of the Schwinger model in Eq. (7), we first identify the time range where a given number of cycles (see Fig. 2) yields a good approximation of the full RK4 result using the IBM's simulator. For example, we find that up to $t = 0.5$, 1 cycle is sufficient for the parameters chosen in the main text, Fig. 4. For larger values of t, we switch to 2 cycles and
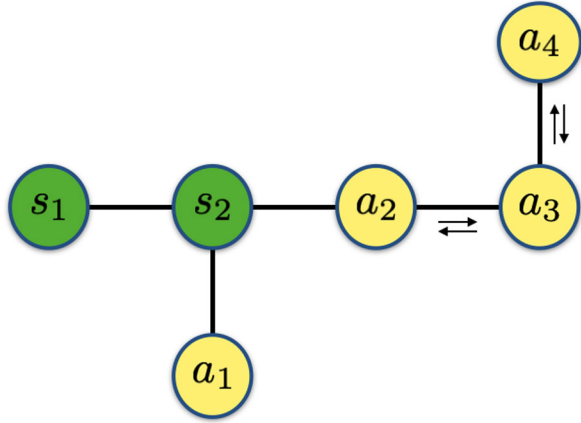
FIG. 6. Configuration of system $s_{1,2}$ and ancilla a_{1-4} qubits on IBMQ. For the third (fourth) cycle/ancilla qubit we use 1 (2) additional swap operations.

eventually up to 3 and 4 cycles. For each time interval we use an appropriate optimization threshold in QSEARCH [114]. The optimization assumes a linear qubit topology with only nearest-neighbor CNOT gates. We verify again with the simulator that the chosen thresholds give an approximation of the RK4 solution within a few percent, i.e. within the error that we can currently achieve on the quantum chip. For four cycles we obtain up to ≈50 CNOT gates. Despite this large number we obtain good results from the IBMQ_MONTREAL device [115] even without applying additional error mitigation techniques. We also verified that we obtain similar results from the IBMQ_TORONTO device [117]. We ran each circuit for 15×8192 shots since the CNOT gate error mitigation using the random identity insertion method of Ref. [112] requires high statistics.

The relevant part of the qubit topology which we use on the IBMQ_MONTREAL device [115] is illustrated in Fig. 6, where the system and ancilla qubits are highlighted with different colors. As mentioned in the main text, we use a different ancilla qubit for every cycle. In our setup the ancilla qubits need to be connected to the system qubit s_2 in Fig. 6. In order to run 3 (4) cycles, we make use of 1 (2) additional swap operations of the ancilla qubits, each of which consist of three CNOT gates. These CNOT gates are included in the CNOT gate error mitigation procedure.

APPENDIX F: VALIDATION OF THE QUANTUM CIRCUIT FOR $N = 4$

In order to further validate the performance of the quantum circuit beyond $N = 2$, we simulate the quantum circuit using the IBMQ (noiseless) simulator for $N = 4$. Figure 7 shows the result along with comparison to the corresponding numerical solutions, which show good agreement.
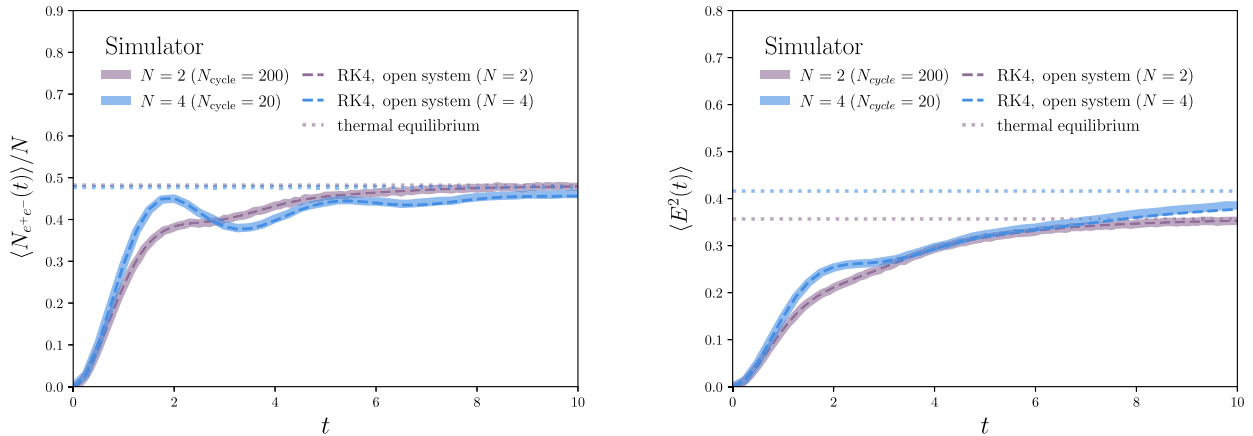

FIG. 7. Quantum simulation of nonequilibrium dynamics in the Schwinger model: $\langle N_{e^+e^-}\rangle$ and $\langle E^2\rangle$ using the quantum circuit for $N = 2$ and $N = 4$, along with numerical solution (RK4). The same values of the parameters are used as in Fig. 5.

APPENDIX G: VOLUME DEPENDENCE FOR $\langle N_{e^+e^-}\rangle$

In order to accompany the volume dependence of $\langle E^2\rangle$ shown in Fig. 5, we plot the average number of electron-positron pairs as a function of N for fixed lattice spacing $a = 1$ in Fig. 8.
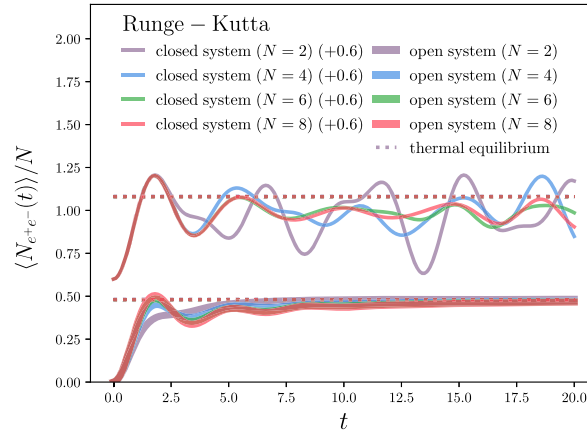

FIG. 8. Numerical solution of nonequilibrium dynamics in the Schwinger model: $\langle N_{e^+e^-}\rangle$ up to $N = 8$. The same values of the parameters are used as in Fig. 5.

[1] M. Devoret and R. Schoelkopf, Superconducting circuits for quantum information: An outlook, Science **339**, 1169 (2013).

[2] M. Kjaergaard, M. E. Schwartz, J. Braumller, P. Krantz, J. I.-J. Wang, S. Gustavsson, and W. D. Oliver, Superconducting qubits: Current state of play, Annu. Rev. Condens. Matter Phys. **11**, 369 (2020).

[3] C. D. Bruzewicz, J. Chiaverini, R. McConnell, and J. M. Sage, Trapped-ion quantum computing: Progress and challenges, Appl. Phys. Rev. **6**, 021314 (2019).

[4] F. Arute, K. Arya, R. Babbush, D. Bacon, J. C. Bardin, R. Barends, R. Biswas, S. Boixo, F. G. S. L. Brandao, and D. A. e. a. Buell, Quantum supremacy using a programmable superconducting processor, Nature (London) **574**, 505 (2019).

[5] L. Bassman, K. Liu, A. Krishnamoorthy, T. Linker, Y. Geng, D. Shebib, S. Fukushima, F. Shimojo, R. K. Kalia, A. Nakano, and P. Vashishta, Towards simulation of the dynamics of materials on quantum computers, Phys. Rev. B **101**, 184305 (2020).

[6] A. Smith, M. S. Kim, F. Pollmann, and J. Knolle, Simulating quantum many-body dynamics on a current digital quantum computer, npj Quantum Inf. **5**, 106 (2019).

[7] J. Preskill, Quantum computing in the NISQ era and beyond, Quantum **2**, 79 (2018).

[8] D. B. Kaplan, N. Klco, and A. Roggero, Ground states via spectral combing on a quantum computer, arXiv: 1709.08250.

[9] J. Preskill, Simulating quantum field theory with a quantum computer, Proc. Sci. LATTICE2018 (**2018**) 024. [arXiv:1811.10085].

[10] H. Lamm and S. Lawrence, Simulation of Nonequilibrium Dynamics on a Quantum Computer, Phys. Rev. Lett. **121**, 170501 (2018).

[11] E. Dumitrescu, A. McCaskey, G. Hagen, G. Jansen, T. Morris, T. Papenbrock, R. Pooser, D. Dean, and P. Lougovski, Cloud Quantum Computing of an Atomic Nucleus, Phys. Rev. Lett. **120**, 210501 (2018).

[12] A. Roggero, A. C. Li, J. Carlson, R. Gupta, and G. N. Perdue, Quantum computing for neutrino-nucleus scattering, Phys. Rev. D **101**, 074038 (2020).

[13] C. W. Bauer, W. A. De Jong, B. Nachman, and D. Provasoli, Quantum Algorithm for High Energy Physics Simulations, Phys. Rev. Lett. **126**, 062001 (2021).

[14] N. Mueller, A. Tarasov, and R. Venugopalan, Deeply inelastic scattering structure functions on a hybrid quantum computer, Phys. Rev. D **102**, 016007 (2020).

[15] A. Y. Wei, P. Naik, A. W. Harrow, and J. Thaler, Quantum algorithms for jet clustering, Phys. Rev. D **101**, 094015 (2020).

[16] E. T. Holland, K. A. Wendt, K. Kravvaris, X. Wu, W. Erich Ormand, J. L. DuBois, S. Quaglioni, and F. Pederiva, Optimal control for the quantum simulation of nuclear dynamics, Phys. Rev. A **101**, 062307 (2020).

[17] N. Klco, J. R. Stryker, and M. J. Savage, SU(2) non-Abelian gauge field theory in one dimension on digital quantum computers, Phys. Rev. D **101**, 074512 (2020).

[18] A. Avkhadiev, P. Shanahan, and R. Young, Accelerating Lattice Quantum Field Theory Calculations via Interpolator Optimization Using Noisy Intermediate-Scale Quantum Computing, Phys. Rev. Lett. **124**, 080501 (2020).

[19] W. A. De Jong, M. Metcalf, J. Mulligan, M. Płoskoń, F. Ringer, and X. Yao, Quantum simulation of open quantum systems in heavy-ion collisions, Phys. Rev. D **104**, L051501 (2021).

[20] J. Liu and Y. Xin, Quantum simulation of quantum field theories as quantum chemistry, J. High Energy Phys. 2012 (2020) 011.

[21] M. Kreshchuk, W. M. Kirby, G. Goldstein, H. Beauchemin, and P. J. Love, Quantum simulation of quantum field theory in the light-front formulation, Phys. Rev. A **105**, 032418 (2022).

[22] Z. Davoudi, I. Raychowdhury, and A. Shaw, Search for efficient formulations for Hamiltonian simulation of non-Abelian lattice gauge theories, Phys. Rev. D **104**, 074505 (2021).

[23] R. A. Briceño, J. V. Guerrero, M. T. Hansen, and A. M. Sturzu, Role of boundary conditions in quantum computations of scattering observables, Phys. Rev. D **103**, 014506 (2021).

[24] M. G. Echevarria, I. L. Egusquiza, E. Rico, and G. Schnell, Quantum simulation of light-front parton correlators, Phys. Rev. D **104**, 014512 (2021).

[25] C. C. Chang, C.-C. Chen, C. Koerber, T. S. Humble, and J. Ostrowski, Integer programming from quantum annealing and open quantum systems, arXiv:2009.11970.

[26] J. Hubisz, B. Sambasivam, and J. Unmuth-Yockey, Quantum algorithms for open lattice field theory, Phys. Rev. A **104**, 052420 (2021).

[27] T. D. Cohen, H. Lamm, S. Lawrence, and Y. Yamauchi, Quantum algorithms for transport coefficients in gauge theories, Phys. Rev. D **104**, 094514 (2021).

[28] J. a. Barata and C. A. Salgado, A quantum strategy to compute the jet quenching parameter $\hat{q}$, Eur. Phys. J. C **81**, 862 (2021).

[29] S. Ramírez-Uribe, A. E. Rentería-Olivo, G. Rodrigo, G. F. R. Sborlini, and L. Vale Silva, Quantum algorithm for Feynman loop integrals, J. High Energy Phys. 05 (2022) 100.

[30] T. Li, X. Guo, W. K. Lai, X. Liu, E. Wang, H. Xing, D.-B. Zhang, and S.-L. hu, Partonic structure by quantum computing, Phys. Rev. D **105**, L111502 (2022).

[31] J. B. Kogut and L. Susskind, Hamiltonian formulation of Wilson's lattice gauge theories, Phys. Rev. D **11**, 395 (1975).

[32] S. P. Jordan, K. S. M. Lee, and J. Preskill, Quantum computation of scattering in scalar quantum field theories, Quantum Inf. Comput. **14**, 1014 (2014).

[33] S. P. Jordan, K. S. Lee, and J. Preskill, Quantum algorithms for quantum field theories, Science **336**, 1130 (2012).

[34] S. P. Jordan, K. S. M. Lee, and J. Preskill, Quantum algorithms for fermionic quantum field theories, arXiv:1404.7115.

[35] S. P. Jordan, H. Krovi, K. S. M. Lee, and J. Preskill, BQP-completeness of scattering in scalar quantum field theory, Quantum **2**, 44 (2018).

[36] D. Horn, Finite matrix models with continuous local gauge invariance, Phys. Lett. **100B**, 149 (1981).

[37] P. Orland and D. Rohrlich, Lattice gauge magnets: Local isospin from spin, Nucl. Phys. **B338**, 647 (1990).

[38] S. Chandrasekharan and U. J. Wiese, Quantum link models: A discrete approach to gauge theories, Nucl. Phys. **B492**, 455 (1997).

[39] U.-J. Wiese, Ultracold quantum gases and lattice systems: Quantum simulation of lattice gauge theories, Ann. Phys. (Berlin) **525**, 777 (2013).

[40] C. Muschik, M. Heyl, E. Martinez, T. Monz, P. Schindler, B. Vogell, M. Dalmonte, P. Hauke, R. Blatt, and P. Zoller, U(1) Wilson lattice gauge theories in digital quantum simulators, New J. Phys. **19**, 103020 (2017).

[41] E. A. Martinez et al., Real-time dynamics of lattice gauge theories with a few-qubit quantum computer, Nature (London) **534**, 516 (2016).

[42] E. Ercolessi, P. Facchi, G. Magnifico, S. Pascazio, and F. V. Pepe, Phase transitions in Z_n gauge models: Towards quantum simulations of the Schwinger-Weyl QED, Phys. Rev. D **98**, 074503 (2018).

[43] N. Klco, E. Dumitrescu, A. McCaskey, T. Morris, R. Pooser, M. Sanz, E. Solano, P. Lougovski, and M. Savage, Quantum-classical computation of Schwinger model dynamics using quantum computers, Phys. Rev. A **98**, 032331 (2018).

[44] I. Raychowdhury and J. R. Stryker, Solving Gauss's Law on digital quantum computers with loop-string-hadron digitization, Phys. Rev. Research **2**, 033039 (2020).

[45] N. Klco and M. J. Savage, Digitization of scalar fields for quantum computing, Phys. Rev. A **99**, 052335 (2019).

[46] G. Magnifico, M. Dalmonte, P. Facchi, S. Pascazio, F. V. Pepe, and E. Ercolessi, Real time dynamics and confinement in the $\mathbb{Z}_n$ Schwinger-Weyl lattice model for $1+1$ QED, Quantum **4**, 281 (2020).

[47] B. Chakraborty, M. Honda, T. Izubuchi, Y. Kikuchi, and A. Tomiya, Digital quantum simulation of the Schwinger model with topological term via adiabatic state preparation, Phys. Rev. D **105**, 094503 (2022).

[48] A. F. Shaw, P. Lougovski, J. R. Stryker, and N. Wiebe, Quantum algorithms for simulating the lattice Schwinger model, Quantum **4**, 306 (2020).

[49] D. E. Kharzeev and Y. Kikuchi, Real-time chiral dynamics from a digital quantum simulation, Phys. Rev. Research **2**, 023342 (2020).

[50] K. Ikeda, D. E. Kharzeev, and Y. Kikuchi, Real-time dynamics of Chern-Simons fluctuations near a critical point, Phys. Rev. D **103**, L071502 (2021).

[51] A. Alexandru, P. F. Bedaque, S. Harmalkar, H. Lamm, S. Lawrence, and N. C. Warrington (NuQS Collaboration), Gluon field digitization for quantum computers, Phys. Rev. D **100**, 114501 (2019).

[52] J. a. Barata, N. Mueller, A. Tarasov, and R. Venugopalan, Single-particle digitization strategy for quantum computation of a ϕ^4 scalar field theory, Phys. Rev. A **103**, 042410 (2021).

[53] S. Harmalkar, H. Lamm, and S. Lawrence (NuQS Collaboration), Quantum simulation of field theories without state preparation, arXiv:2001.11490.

[54] C. W. Bauer, M. Freytsis, and B. Nachman, Simulating Collider Physics on Quantum Computers Using Effective Field Theories, Phys. Rev. Lett. **127**, 212001 (2021).

[55] A. Ciavarella, N. Klco, and M. J. Savage, A trailhead for quantum simulation of SU(3) Yang-Mills lattice gauge

theory in the local multiplet basis, Phys. Rev. D **103**, 094501 (2021).

[56] M. C. Bañuls *et al.*, Simulating lattice gauge theories within quantum technologies, Eur. Phys. J. D **74**, 165 (2020).

[57] I. C. Clot *et al.*, Opportunities for nuclear physics & quantum information science, in *Intersections between Nuclear Physics and Quantum Information*, edited by I. C. Clot and M. R. Dietrich (2019), arXiv:1903.05453.

[58] D.-B. Zhang, H. Xing, H. Yan, E. Wang, and S.-L. Zhu, Selected topics of quantum computing for nuclear physics, Chin. Phys. B **30**, 020306 (2021).

[59] K. Temme, T. J. Osborne, K. G. Vollbrecht, D. Poulin, and F. Verstraete, Quantum metropolis sampling, Nature (London) **471**, 87 (2011).

[60] M. Motta, C. Sun, A. T. Tan, M. J. ORourke, E. Ye, A. J. Minnich, F. G. Brandao, and G. K.-L. Chan, Determining eigenstates and thermal states on a quantum computer using quantum imaginary time evolution, Nat. Phys. **16**, 205 (2020).

[61] C. Zalka, Simulating quantum systems on a quantum computer, Proc R. Soc. A **454**, 313 (1998).

[62] B. M. Terhal and D. P. DiVincenzo, Problem of equilibration and the computation of correlation functions on a quantum computer, Phys. Rev. A **61**, 022301 (2000).

[63] H. Wang, S. Ashhab, and F. Nori, Quantum algorithm for simulating the dynamics of an open quantum system, Phys. Rev. A **83**, 062317 (2011).

[64] M. Metcalf, J. E. Moussa, W. A. de Jong, and M. Sarovar, Engineered thermalization and cooling of quantum many-body systems, Phys. Rev. Research **2**, 023214 (2020).

[65] C. Young and K. Dusling, Quarkonium above deconfinement as an open quantum system, Phys. Rev. C **87**, 065206 (2013).

[66] Y. Akamatsu and A. Rothkopf, Stochastic potential and quantum decoherence of heavy quarkonium in the quark-gluon plasma, Phys. Rev. D **85**, 105011 (2012).

[67] P. B. Gossiaux and R. Katz, Upsilon suppression in the Schrdinger–Langevin approach, Nucl. Phys. **A956**, 737 (2016).

[68] N. Brambilla, M. A. Escobedo, J. Soto, and A. Vairo, Heavy quarkonium suppression in a fireball, Phys. Rev. D **97**, 074009 (2018).

[69] X. Yao and T. Mehen, Quarkonium in-medium transport equation derived from first principles, Phys. Rev. D **99**, 096028 (2019).

[70] T. Miura, Y. Akamatsu, M. Asakawa, and A. Rothkopf, Quantum Brownian motion of a heavy quark pair in the quark-gluon plasma, Phys. Rev. D **101**, 034011 (2020).

[71] R. Sharma and A. Tiwari, Quantum evolution of quarkonia with correlated and uncorrelated noise, Phys. Rev. D **101**, 074004 (2020).

[72] V. Vaidya and X. Yao, Transverse momentum broadening of a jet in quark-gluon plasma: An open quantum system EFT, J. High Energy Phys. 10 (2020) 024.

[73] X. Yao, W. Ke, Y. Xu, S. A. Bass, and B. Mller, Coupled Boltzmann transport equations of heavy quarks and quarkonia in quark-gluon plasma, J. High Energy Phys. 01 (2021) 046.

[74] X. Yao and T. Mehen, Quarkonium semiclassical transport in quark-gluon plasma: Factorization and quantum correction, J. High Energy Phys. 02 (2021) 062.

[75] Y. Akamatsu, Quarkonium in quark-gluon plasma: Open quantum system approaches re-examined, Prog. Part. Nucl. Phys. **123**, 103932 (2022).

[76] N. Brambilla, M. A. Escobedo, M. Strickland, A. Vairo, P. Vander Griend, and J. H. Weber, Bottomonium suppression in an open quantum system using the quantum trajectories method, J. High Energy Phys. 05 (2021) 136.

[77] X. Yao, Open quantum systems for quarkonia, Int. J. Mod. Phys. A **36**, 2130010 (2021),

[78] A. Lehmann and A. Rothkopf, Proper static potential in classical lattice gauge theory at finite T, J. High Energy Phys. 07 (2021) 067.

[79] D. Neill, The edge of jets and subleading non-global logs, arXiv:1508.07568.

[80] N. Armesto, F. Dominguez, A. Kovner, M. Lublinsky, and V. Skokov, The color glass condensate density matrix: Lindblad evolution, entanglement entropy and Wigner functional, J. High Energy Phys. 05 (2019) 025.

[81] M. Li and A. Kovner, JIMWLK evolution, Lindblad equation and quantum-classical correspondence, J. High Energy Phys. 05 (2020) 036.

[82] D. Boyanovsky, Effective field theory during inflation: Reduced density matrix and its quantum master equation, Phys. Rev. D **92**, 023527 (2015).

[83] C. P. Burgess, R. Holman, and G. Tasinato, Open EFTs, IR effects & late-time resummations: Systematic corrections in stochastic inflation, J. High Energy Phys. 01 (2016) 153.

[84] S. Shandera, N. Agarwal, and A. Kamal, Open quantum cosmological system, Phys. Rev. D **98**, 083535 (2018).

[85] M. Zarei, N. Bartolo, D. Bertacca, S. Matarrese, and A. Ricciardone, Non-Markovian open quantum system approach to the early universe: I. Damping of gravitational waves by matter, Phys. Rev. D **104**, 083508 (2021).

[86] T. Cohen and D. Green, Soft de Sitter effective theory, J. High Energy Phys. 12 (**2020**) 041.

[87] T. Binder, B. Blobel, J. Harz, and K. Mukaida, Dark matter bound-state formation at higher order: A non-equilibrium quantum field theory approach, J. High Energy Phys. 09 (2020) 086.

[88] R. Cleve and C. Wang, Efficient quantum algorithms for simulating Lindblad evolution, in *Proceedings of the 44th International Colloquium on Automata, Languages, and Programming (ICALP 2017)*, arXiv:1612.09512.

[89] J. Berges, M. P. Heller, A. Mazeliauskas, and R. Venugopalan, Thermalization in QCD: Theoretical approaches, phenomenological applications, and interdisciplinary connections, Rev. Mod. Phys. **93**, 035003 (2021).

[90] J. S. Schwinger, Gauge invariance and mass. II., Phys. Rev. **128**, 2425 (1962).

[91] S. R. Coleman, R. Jackiw, and L. Susskind, Charge shielding and quark confinement in the massive Schwinger model, Ann. Phys. (N.Y.) **93**, 267 (1975).

[92] D. E. Kharzeev and F. Loshaj, Jet energy loss and fragmentation in heavy ion collisions, Phys. Rev. D **87**, 077501 (2013).

[93] F. Loshaj and D. E. Kharzeev, Soft photon production from real-time dynamics of jet fragmentation, Nucl. Phys. **A931,** 712 (2014).

[94] E. A. Calzetta and B.-L. B. Hu, *Nonequilibrium Quantum Field Theory*, Cambridge Monographs on Mathematical Physics (Cambridge University Press, Cambridge, England, 2008).

[95] S. R. Coleman, More about the massive Schwinger model, Ann. Phys. (N.Y.) **101,** 239 (1976).

[96] Z.-Y. Zhou, G.-X. Su, J. C. Halimeh, R. Ott, H. Sun, P. Hauke, B. Yang, Z.-S. Yuan, J. Berges, and J.-W. Pan, Thermalization dynamics of a gauge theory on a quantum simulator, Science **377,** eabl6277 (2022).

[97] A. Casher, J. B. Kogut, and L. Susskind, Vacuum Polarization and the Quark Parton Puzzle, Phys. Rev. Lett. **31,** 792 (1973).

[98] T. Banks, L. Susskind, and J. B. Kogut, Strong coupling calculations of lattice gauge theories: $(1 + 1)$-Dimensional exercises, Phys. Rev. D **13,** 1043 (1976).

[99] P. Jordan and E. P. Wigner, About the Pauli exclusion principle, Z. Phys. **47,** 631 (1928).

[100] A. Kossakowski, On quantum statistical mechanics of non-Hamiltonian systems, Rep. Math. Phys. **3,** 247 (1972).

[101] G. Lindblad, On the generators of quantum dynamical semigroups, Commun. Math. Phys. **48,** 119 (1976).

[102] V. Gorini, A. Frigerio, M. Verri, A. Kossakowski, and E. Sudarshan, Properties of quantum Markovian master equations, Rep. Math. Phys. **13,** 149 (1978).

[103] A. O. Caldeira and A. J. Leggett, Influence of Dissipation on Quantum Tunneling in Macroscopic Systems, Phys. Rev. Lett. **46,** 211 (1981).

[104] M. A. Nielsen and I. L. Chuang, *Quantum Computation and Quantum Information: 10th Anniversary Edition* (Cambridge University Press, Cambridge, England, 2010).

[105] Z. Hu, R. Xia, and S. Kais, A quantum algorithm for evolving open quantum dynamics on quantum computing devices, Sci. Rep. **10,** 3301 (2020).

[106] K. Head-Marsden, S. Krastanov, D. A. Mazziotti, and P. Narang, Capturing non-Markovian dynamics on near-term quantum computers, Phys. Rev. Research **3,** 013182 (2021).

[107] P. Gupta and C. M. Chandrashekar, Optimal quantum simulation of open quantum systems (2020), arXiv:2012.07540.

[108] L. Del Re, B. Rost, A. F. Kemper, and J. K. Freericks, Driven-dissipative quantum mechanics on a lattice: Simulating a fermionic reservoir on a quantum computer, Phys. Rev. B **102,** 125112 (2020).

[109] N. Ramusat and V. Savona, A quantum algorithm for the direct estimation of the steady state of open quantum systems (2020), 10.22331/q-2021-02-22-399.

[110] M. Metcalf, E. Stone, K. Klymko, A. F. Kemper, M. Sarovar, and W. A. de Jong, Quantum Markov chain Monte Carlo with digital dissipative dynamics on quantum computers (2021), arXiv: 2103.03207.

[111] A. e. a. Héctor Abraham, Qiskit: An open-source framework for quantum computing (2019), https://zenodo.org/record/2562111/export/hx#.Yxj7G-zMLPA.

[112] A. He, B. Nachman, W. A. de Jong, and C. W. Bauer, Zero-noise extrapolation for quantum-gate error mitigation with identity insertions, Phys. Rev. A **102,** 012426 (2020).

[113] A. G. Rattew, Y. Sun, P. Minssen, and M. Pistoia, Quantum simulation of Galton machines using mid-circuit measurement and reuse (2021), arXiv:2009.06601.

[114] A. Hashim, R. K. Naik, A. Morvan, J.-L. Ville, B. Mitchell, J. M. Kreikebaum, M. Davis, E. Smith, C. Iancu, K. P. O'Brien, I. Hincks, J. J. Wallman, J. Emerson, and I. Siddiqi, Randomized Compiling for Scalable Quantum Computing on a Noisy Superconducting Quantum Processor, Phys. Rev. X **11,** 041039 (2021).

[115] 27-qubit backend: IBM Q team, IBM Q Montreal backend specification v1.9.11, retrieved from https://quantum-computing.ibm.com (2021).

[116] W. Feller, *An Introduction to Probability Theory and Its Applications*, 2nd ed. (Wiley, New York, 1971), Vol. 2.

[117] 27-qubit backend: IBM Q team, IBM Q Toronto backend specification v1.4.24, retrieved from https://quantum-computing.ibm.com.